

Numerical Simulation of Gas-liquid Two-phase Flow in Emergency Rescue Drainage Pump Based on MUSIG Model

W. Cao¹, X. Yang^{1†}, H. Wang² and X. Leng²

¹ *Research Center of Fluid Machinery Engineering and Technology, Jiangsu University, Zhenjiang, People's Republic of China*

² *Wenling Fluid Machinery Technology Institute of Jiangsu University, Wenling, Zhejiang 317500, People's Republic of China*

†Corresponding Author Email: 2212111009@stmail.ujs.edu.cn

ABSTRACT

To investigate the gas-liquid two-phase flow characteristics in an emergency rescue drainage pump, the MUSIG model was adopted to analyze the effect of the gas phase on the internal flow characteristics of the pump. The results show that the gas phase predominantly accumulated in the impeller region, with significant tendencies for large diameter bubbles to fragment into smaller diameter bubbles. The bubbles of the impeller blades converged towards the middle zone of the blade near the hub, forming an air pocket that obstructed the flow passage through the impeller. Such findings ultimately resulted in a loss of pump performance. Moreover, as the diameter of inlet bubble increased, there was a greater tendency for the gas phase to converge into a concentration distribution, leading to unfavorable flow conditions in the pump. This phenomenon ultimately led to a decline in pump performance and may have resulted in the loss of water conveyance functionality. Meanwhile, the Ω method was used to investigate the vortex flow within the drainage pump under different gas contents. As the inlet gas volume fraction increased, the vortex area expanded and the vortex tended to fragment into multiple smaller pieces, resulting in the formation of more complex structures.

Article History

Received October 25, 2023

Revised February 28, 2024

Accepted March 14, 2024

Available online May 29, 2024

Keywords:

Gas-liquid two-phase flow

MUSIG model

Gas phase diameter

Vortex

1. INTRODUCTION

Emergency rescue drainage pumps are extensively employed in agricultural water supply for irrigation, as well as in urban, industrial, and mining drainage systems. This widespread adoption can be attributed to its convenient portability and robust water conveyance capabilities. Such pumps possess are designed to operate as integrated electromechanical systems, capable of submerging into water while exhibiting the characteristics commonly associated with axial flow pumps. A dual-sealing structure is adopted for the pump motor, which is integrated with the pump body, thereby significantly reducing the overall size of the pump. This design minimizes unnecessary connecting components, greatly enhancing the reliability of the pump assembly. During the drainage operation, a common issue arises from insufficient submersion depth, leading to the introduction of gas into the medium. This transforms the flow inside the pump from a single fluid into a complex gas-liquid two-phase flow. Owing to the influence of the hydraulic structure of the axial flow pump and the high-speed and portable design, there is a propensity to generate local pressure reductions and accumulate bubbles within the

emergency rescue drainage pump. In severe instances, the gas will block the flow channel, causing a gas lock that will make the pump lose water delivery function. Further, the unstable interplay between gas and liquid can disrupt the vortex structure within the pump, resulting in significant energy loss.

The Eulerian-Eulerian two-fluid model (TFM) has been extensively employed for numerical simulations within pumps (Wu et al., 1998; Kim et al., 2015). Chen et al. (2019) first applied the population balance model to investigate the internal flow inside a submersible electric pump. The model effectively captured phenomena related to bubble aggregation and fragmentation in the two-phase flow system. On the basis of the aforementioned research, Zhang et al. (2020a) and Yan et al. (2020) applied the Population Balance Model (PBM) to investigate distinct aspects of pump behavior. Zhang et al. (2020a) utilized the PBM model to analyze the variation of bubble diameter within a vane pump, while Yan et al. examined pressure and gas phase distribution within the pump. Lo (1996) further proposed the multiple size groups (MUSIG) model, which discretizes the gas phase into several bubble groups based on their size. Subsequently, population equilibrium

Nomenclature			
n_i	number of bubbles in the i th group in the unit volume	θ_{ij}^x	collision frequency of bubbles caused by bubble velocity difference
U_i	speed of bubble movement, S_{ph} denotes the change in the number of bubbles caused	θ_{ij}^b	collision frequency of bubbles caused by turbulent eddies
B_B	increase in the density of the i th group of bubbles caused by bubble bursting.	θ_{ij}^s	collision frequency of bubbles caused by laminar shear
D_B	decrease in the density of the i th group of bubbles caused by bubble bursting	η_{ij}	likelihood of bubble aggregation resulting from collision.
B_C	increase in the density of the i th group of bubbles caused by bubble aggregation	f_{BV}	random fragmentation volume fraction
D_C	decrease in the density of the i th group of bubbles caused by bubble aggregation	ζ	size of the vortex in the inertial subinterval of isotropic turbulence
S_{ph}	change in the number of bubbles caused	F_B	correction factor
ε_c	continuous phase vortex dissipation rate	σ	surface tension coefficient
u	components of the velocity in the directions x	v	components of the velocity in the directions y
w	components of the velocity in the directions z	ω	vorticity of a fluid micro cluster
R_ω	rotating vorticity part	S_ω	non-rotating vorticity part
Ω	vortex identification method	S_p	radial coefficient of the blade
r	radius	r_t	rim radius
r_h	radius of the hub	P_{out}	drainage pump export total pressure
P_{in}	drainage pump import total pressure	ρ_{mix}	gas-liquid mixture density
T	torque	H^*	dimensionless parameter
$IGVF$	inlet gas volume fraction	P^*	dimensionless parameter
n	rotational speed in revolutions per minute	D_2	the impeller outlet diameter in meters
p	pressure in Pascals	ρ	density of the two-phase gas-liquid flow in kilograms per cubic meter
u_2	circumferential velocity at the impeller outlet in meters per second	Q_g	gas volume flow rate
Q_l	liquid volume flow rate	D_{ab}	average bubble diameter
P_i	the absolute pressure at each axial section (z-x plane) along the pump's axial direction.		

equations were established for each bubble group. [Pineda et al. \(2016\)](#) investigated gas-liquid two-phase flow in a pump utilizing the Volume of Fluid model. They identified the correlation between pump head and inlet gas volume fraction, noting that with increased rotational speed, the gas volume fraction within the pump also increased. [Liu et al. \(2022\)](#) initiated their study by examining the Weber number and subsequently developed correlations between gas phase diameter and parameters such as speed and gas content, leveraging the critical Weber number. [Xu et al. \(2023\)](#) explored the pressure pulsation rule of the gas content on the blade of a diffused vane type aviation fuel pump, finding that the bubbles were mainly distributed in the pressure sides. As the gas volume fraction increased, it extended gradually towards the suction sides of the blades, eventually diffusing into the flow channel of the impeller.

In the 1990's, scholars ([Chong et al., 1990](#); [Levy et al., 1990](#); [Zhou et al., 1999](#)) introduced vortex identification methods that did not rely on coordinate transformations, including the Q-criterion, λ_2 , and Δ -criterion. [Wang et al. \(2019\)](#) employed the relative vorticity transport equation to investigate the leakage vortex occurring at the blade tip. Their analysis uncovered that this vortex within the blade tip gap could significantly impact pump performance. Considering that the previously mentioned vortex identification methods were highly sensitive to threshold selection, [Liu et al. \(2016\)](#) introduced the Omega (Ω)

vortex identification method. This approach was less affected by threshold choices and could effectively capture all kinds of vortices. To investigate the influence of three vortex structures (longitudinal, axial, and radial) on turbulent flow within a pump, [Zhang et al. \(2020b\)](#) employed the Ω method. They discovered that the longitudinal vortex enhanced momentum exchange. Conversely, the axial and radial vortices opposed this exchange process, leading to a reduction in pump efficiency. [Li et al. \(2016\)](#) conducted vortex studies based on vortex theory for small pump turbines characterized by high efficiency and high flow rates. Their investigation revealed that the vortex in the impeller region was significantly impacted by the flow rate. Further, the distribution of vortices in the high vortex region was influenced by adverse fluid flow generated by the vortex.

In previous studies, there has been a scarcity of research on the internal flow characteristics of high-speed emergency rescue drainage pumps operating under gas-liquid flow conditions. To explore the impacts of gas content on both the flow field and the external characteristics of the pump, the MUSIG model was employed to deduce the distribution of the gas phase and the laws governing bubble movement in the flow channel of the emergency rescue drainage pump. Subsequently, using the Ω method, the mechanism of unsteady flow in emergency rescue drainage pumps for two-phase flow was examined. The research findings of the present study can

address the existing research gap in the field of gas-liquid flow in drainage pumps, providing theoretical guidance for the design of drainage pumps applicable to gas-liquid two-phase flow.

2. GENERAL GUIDELINES

2.1 MUSIG Model

This model was developed based on a multi-scale interfacial and geometrical framework, which integrates the effects of various factors such as surface tension and viscosity. In the MUSIG model, the fluid system is segregated into two segments: the continuous phase and the poly-dispersed fluid. Their macroscopic dynamics and microscopic interactions are evaluated independently.

In contrast to the TFM model, the MUSIG model incorporates variations in the diameter of gas particles and segregates gas bubbles of different scales into various size groups. The MUSIG model simulates each size group individually, thereby effectively resolving the issues arising from the diversity of physical phenomena and scale variability. Meanwhile, the MUSIG model integrates the Prince-Blanch model (Prince & Blanch 1990) with the Luo-Svendsen model (Luo & Svendsen 1996) to elucidate the mechanisms underlying bubble aggregation and fragmentation.

2.2 Population Balance Equation

This equation characterizes the continuous evolution of the particle distribution across time and space in a multiphase flow system. A transfer equation for the number density of bubbles has been formulated to anticipate the effects of bubble collision on bubble size, as well as to predict the local average density distribution of bubble diameters. For bubbles of group i , the equation can be expressed as:

$$\frac{\partial n_i}{\partial t} + \nabla \cdot (\bar{U}_i n_i) = (B_B - D_B + B_C - D_C) + (S_{ph}) \quad (1)$$

where n_i represents the number of bubbles in the i th group in the unit volume; U_i indicates the speed of bubble movement; S_{ph} denotes the change in the number of bubbles caused; B_B and D_B represent the increase and decrease in the density caused by bubble bursting. Additionally, B_C and D_C represent the increase and decrease in the density caused by bubble aggregation.

2.3 Bubble Aggregation Model

The Prince-Blanch model assumes that the bubble aggregation rate is affected by the collision frequency and the probability of collisions leading to aggregation. The mass-based aggregation rate is calculated as follows:

$$Q(m_i; m_j) = (\theta_{ij}^T + \theta_{ij}^B + \theta_{ij}^S) \eta_{ij} \quad (2)$$

Where: θ_{ij}^T , θ_{ij}^B , θ_{ij}^S represent the collision frequency of bubbles caused by turbulent eddies, bubble velocity difference and laminar shear, respectively, while η_{ij} denotes the likelihood of bubble aggregation due to collision.

2.4 Bubble Breakup Model

The Luo-Svendsen model assumes that all bubbles undergo binary fragmentation. The fragmentation is influenced by the vortex, which triggers oscillations when the length scale of the vortex is smaller than the bubble's diameter. The fragmentation rate of the bubbles, measured by mass, is determined by using the following formula:

$$g(m_i; f_{BV} m_i) = 0.923 F_B (1 - r_d) \left(\frac{\varepsilon_c}{d_i^2} \right)^{1/3} \int_{\xi_{\min}}^1 \frac{(1 + \xi)^2}{\xi^{3/11}} \exp(-\chi) d\xi \quad (3)$$

$$\chi = \frac{12 \left[f_{BV}^{2/3} + (1 - f_{BV})^{2/3} - 1 \right] \sigma}{\beta \rho_c \varepsilon_c^{2/3} d_i^{5/3} \xi^{3/11}} \quad (4)$$

where: f_{BV} represents the random fragmentation volume fraction; ξ denotes the size of the vortex of isotropic turbulence, $\xi = \lambda/d_i$; F_B is the correction factor; ε_c denotes the continuous phase vortex dissipation rate; σ is the surface tension coefficient; and β is a constant assigned the value of 2.0.

2.5 Ω Method

The Ω method decomposes the velocity gradient tensor into two components: the symmetric tensor A and the antisymmetric tensor B . These components represent the deformation and rotation, respectively, of a point within the flow field. The definitions of A and B are as follows:

$$\mathbf{A} = \frac{1}{2} (\nabla \mathbf{V} + \nabla \mathbf{V}^T) = \begin{bmatrix} \frac{\partial u}{\partial x} & \frac{1}{2} \left(\frac{\partial v}{\partial x} + \frac{\partial u}{\partial y} \right) & \frac{1}{2} \left(\frac{\partial w}{\partial z} + \frac{\partial u}{\partial x} \right) \\ \frac{1}{2} \left(\frac{\partial v}{\partial x} + \frac{\partial u}{\partial y} \right) & \frac{\partial v}{\partial y} & \frac{1}{2} \left(\frac{\partial w}{\partial y} + \frac{\partial v}{\partial z} \right) \\ \frac{1}{2} \left(\frac{\partial w}{\partial z} + \frac{\partial u}{\partial x} \right) & \frac{1}{2} \left(\frac{\partial w}{\partial y} + \frac{\partial v}{\partial z} \right) & \frac{\partial w}{\partial z} \end{bmatrix} \quad (5)$$

$$\mathbf{B} = \frac{1}{2} (\nabla \mathbf{V} - \nabla \mathbf{V}^T) = \begin{bmatrix} 0 & \frac{1}{2} \left(\frac{\partial u}{\partial y} - \frac{\partial v}{\partial x} \right) & \frac{1}{2} \left(\frac{\partial u}{\partial z} - \frac{\partial w}{\partial x} \right) \\ \frac{1}{2} \left(\frac{\partial v}{\partial x} - \frac{\partial u}{\partial y} \right) & 0 & \frac{1}{2} \left(\frac{\partial v}{\partial z} - \frac{\partial w}{\partial y} \right) \\ \frac{1}{2} \left(\frac{\partial w}{\partial x} - \frac{\partial u}{\partial z} \right) & \frac{1}{2} \left(\frac{\partial w}{\partial y} - \frac{\partial v}{\partial z} \right) & 0 \end{bmatrix} \quad (6)$$

where u , v , and w are the components of the velocity in the directions x , y , and z , respectively. In Liu's approach, the vorticity ω of a fluid micro cluster is decomposed into two components: the rotating part R_ω and the non-rotating part S_ω . The vorticity ω is defined as:

$$\omega = R_\omega + S_\omega \quad (7)$$

Subsequently, a new parameter is introduced to quantify the contribution of the rotating part to the overall vortex size. To prevent a zero denominator, a positive number ε is added. This parameter is as follow:

$$\Omega = \frac{\|\mathbf{B}\|_F^2}{\|\mathbf{A}\|_F^2 + \|\mathbf{B}\|_F^2 + \varepsilon} \quad (8)$$

From Equation (8), the range of values for Ω , $0 \leq \Omega \leq 1$, can be understood as a measure of the concentration of the vortex volume within the rotating part R_ω . In particular, Ω represents the degree of rigidity in fluid motion. When $\Omega > 0.5$, it implies that the norm of the antisymmetric tensor \mathbf{B} is greater than the norm of the symmetric tensor \mathbf{A} . In this case, $\Omega > 0.5$ can serve as a criterion for identifying vortices.

2.6 Basic Control Equations

This section primarily introduces the fundamental control equations employed in the simulation.

The continuity equation can be as follows:

$$\frac{\partial \rho}{\partial t} + \frac{\partial(\rho u)}{\partial x} + \frac{\partial(\rho v)}{\partial y} + \frac{\partial(\rho w)}{\partial z} = 0 \quad (9)$$

Where: ρ represents the density of the fluid.

The momentum conservation equation can be as follows:

$$\frac{\partial(\rho u)}{\partial t} + \text{div}(\rho uu) = \text{div}(\mu \text{grad} u) - \frac{\partial p}{\partial x} + S_u \quad (10)$$

$$\frac{\partial(\rho v)}{\partial t} + \text{div}(\rho vu) = \text{div}(\mu \text{grad} v) - \frac{\partial p}{\partial y} + S_v \quad (11)$$

$$\frac{\partial(\rho w)}{\partial t} + \text{div}(\rho wu) = \text{div}(\mu \text{grad} w) - \frac{\partial p}{\partial z} + S_w \quad (12)$$

where μ represents dynamic viscosity in Pa·s; S_u , S_v and S_w are the generalized source terms for the momentum equation. The described equation is the momentum equation after incorporating shear stress.

2.7 Turbulence Model—SST k- ω

This model is particularly effective for simulating flow separation in adverse pressure gradient conditions. Its formula is as follows:

$$\frac{\partial \rho K}{\partial t} + \frac{\partial \rho K u_j}{\partial x_j} = \frac{\partial}{\partial x_j} \left[(\mu + \sigma_k \mu_t) \frac{\partial K}{\partial x_j} \right] + P_K - \beta^* \rho \omega K \quad (13)$$

$$\frac{\partial \rho \omega}{\partial t} + \frac{\partial \rho \omega u_j}{\partial x_j} = \frac{\partial}{\partial x_j} \left[(\mu + \sigma_\omega \mu_t) \frac{\partial \omega}{\partial x_j} \right] + \frac{\gamma}{v_t} P_K + 2(1 - F_1) \rho \sigma_{\omega 2} \frac{1}{\omega} \frac{\partial K}{\partial x_j} \frac{\partial \omega}{\partial x_j} \quad (14)$$

Where: ω represents the specific rate of dissipation, ν_t is the turbulent eddy viscosity coefficient, and P_K is the turbulence kinetic energy generation coefficient.

3. EXPERIMENTS AND GEOMETRIC MODELS

3.1 Pump Parameters

The whole pump structure is shown in Fig. 1. The fluid enters the drainage pump through the influent chamber from the side, and the axial impeller pressurizes the fluid, finally, the guide vanes rectify the fluid and direct it into the discharge section. The emergency rescue drainage pump, investigated in the present study, was designed with specific parameters: a flow rate of $Q = 0.11 \text{ m}^3/\text{s}$, a designed head of $H = 8.5 \text{ m}$, and operated at a speed of $n = 3000 \text{ r/min}$. The method for describing the rotational motion of impeller can use kinematic quantities such as angular velocity or the number of revolutions per minute of the impeller. The impeller had an outer diameter of 168 mm and a hub diameter of 78.6 mm, with a total of 4 impeller blades. The guide vanes had an inlet diameter of 169 mm, an outlet diameter of 173.5 mm, and were equipped with 6 guide vane blades.

3.2 Grid Division and Grid Independence Verification

As shown in Fig. 2 (a), the water body simulated contained the inlet section, impeller, guide vane, and outlet section. To ensure mesh accuracy and select appropriate y^+ value, the main body mesh utilized a hexahedral meshing approach, while the boundary layer mesh was generated using the BiGeometric method. For wall-bounded turbulence, the SST k- ω function was applied to handle the near-wall region. As shown in Table 1, five different numbers of meshes were used to verify the mesh-independence. From Plan 1 to Plan 5, the grid size of each component inside the pump gradually decreased from 4 to 2. When the number of grid points increased from 2.31 million to 4.24 million, there was an observable upward trend in head. However, once the number of grid points surpassed 4.24 million, the increase in head became less pronounced, and the efficiency exhibited a subtle fluctuation with diminishing magnitude as the number of grid points continued to increase. Considering the need for simulation accuracy and the economy of numerical calculations, a total of 4.24 million grid points was chosen for calculations. Specifically, the numbers of grid points

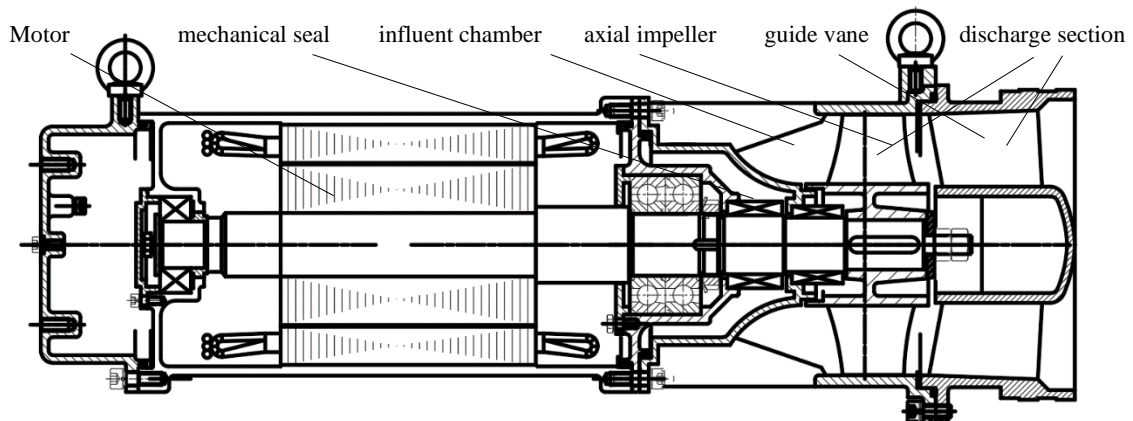


Fig. 1 Emergency rescue drainage pump

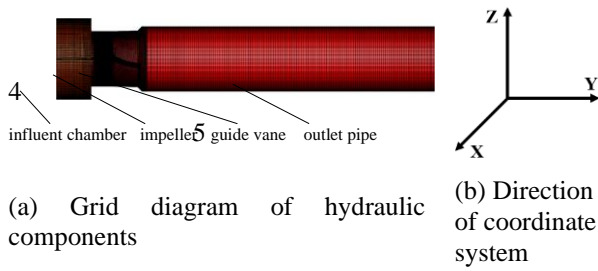


Fig. 2 Grid of emergency rescue drainage pump

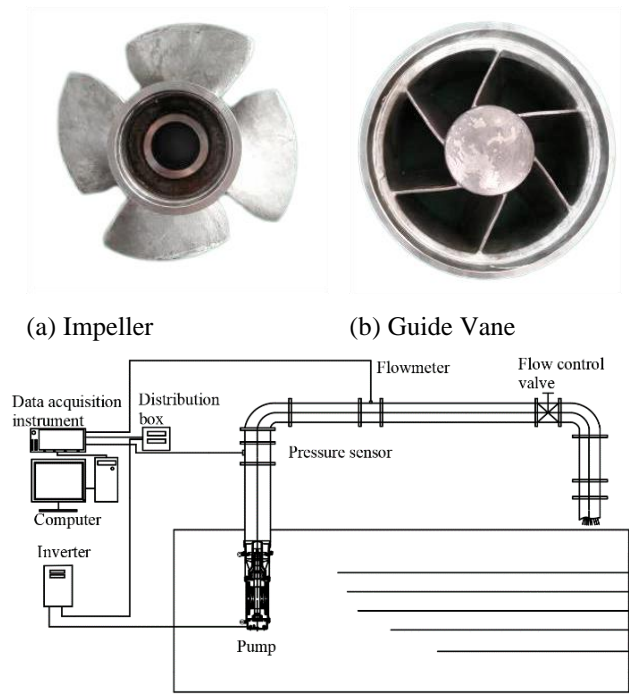
Table 1 Grid independence verification

Scheme	Grid numbers/10 ⁴	Head/m	η /%
1	223	8.96	53.96
2	296	9.02	54.32
3	424	9.11	54.49
4	792	9.14	54.53
5	1142	9.17	54.46

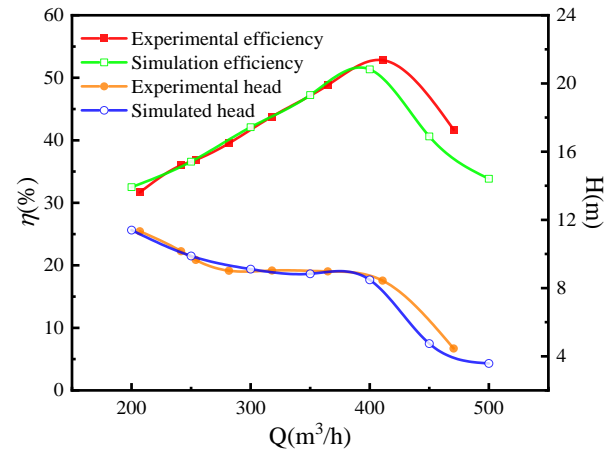
allocated to the influent chamber, impeller, guide vane, and outlet pipe were 987724, 1339740, 1155798 and 761241, respectively. The aspect ratio of the grid in the impeller section remains around 0.8, while in other areas it remains close to 1. Further, the average $y+$ value on the impeller surface was 21.83, and on the guide vane surface, it measured 31.43. Both values met the required standards for simulation accuracy and the numerical stability of the simulation is also guaranteed. For the sake of visual clarity in subsequent image processing, the 3D coordinate system was oriented as depicted in Fig 2(b), with the coordinate origin located at the center of the impeller. Here, η represents efficiency.

5.2 Simulation Settings

The simulation software used in the present study was Ansys CFX. To ensure that the CFL number is between 1 and 10, the transient simulation utilized results calculated at every 3 degrees of impeller rotation, with a non-uniform time step. The duration of the transient simulation covered 10 impeller rotation cycles, equivalent to 0.2 seconds. The fluid medium consisted of a mixture of air and water at 25°C. The inlet boundary condition was configured as a pressure inlet set at 101.325 kPa. The inlet gas volume fraction (IGVF) was specified accordingly. The outlet boundary condition was defined as a mass flow outlet. The fluid was simulated by SST $k-\omega$ turbulence model. The gas phase was treated as an incompressible medium. The bubbles were assumed to be uniformly spherical, and no considerations were made for their deformation or phase transition. The MUSIG model settings were as follows: the gas phase was a multi-discrete fluid, the bubble group was set to 5 groups, the bubble size was equal to the diameter of the discrete distribution, the minimum particle size was 0.5mm, the maximum particle size was 2mm, and the average diameter of the inlet gas phase was set to 1.25mm. To characterize the composition of the initial gas-liquid two-phase working medium, the inlet gas volume fraction was defined as: $IGVF = Q_g / (Q_g + Q_l)$, where Q_g is the gas volume flow rate and Q_l is the same thing of the liquid.



(c) Schematic diagram of the test bench



(d) Comparison of External Characteristics

Fig. 3 External characteristic experiment

3.4 Comparative Analysis of External Characteristic

As depicted in Figs. 3(a) and (b), stainless steel components were employed to manufacture the impeller and guide vane of the emergency rescue drainage pump. As shown in Fig. 3(c), the experimental setup primarily consisted of a drainage pump, variable frequency drive, control valve, pressure sensor, flowmeter, data acquisition instrument, and others. The pump speed was changed by the variable frequency drive, and valves could be used to adjust flow. The outlet pressure was monitored using a pressure sensor. Specifically, the pressure sensor utilized was the WT2000 type, featuring a measurement range of 0 to 1.6 MPa. The flowmeter employed was the LWGY-50A0A3T type turbine flowmeter with a testing accuracy of 0.5%. The data acquisition instrument was the TPA-3A hydraulic machinery comprehensive test apparatus from Jiangsu University. Each case underwent five repeated tests.

Figure 3(d) compares the experimental and simulated data of the pump. The results show a correlation between the simulated and test data for the emergency drainage pump. Under the design flow rate, there was only a 2% difference in head and efficiency between the simulated values and the tested values. Overall, the differences between the simulated and tested values under different flow rates were within acceptable limits, demonstrating that the numerical simulations were relatively accurate and met the specifications for further analysis of internal flow.

4. ANALYSIS OF SIMULATION RESULTS

4.1 Pressure Distribution

Figure 4 shows a comparison of the total pressure profiles of the middle section of the water body under different conditions, which were set at the x-y plane at z = 0. An observation can be made from Fig. 4 (a) that under the conditions of single-phase water, the pressure at the edge of the impeller exceeded 210 kPa, which was higher than the pressure at the same position in Fig. 4 (b). In Fig. 4 (b), there was a small amount of regional pressure in the range of 120-150 kPa near the impeller and guide vane outlet. Typically, the pressure distribution of the drainage pump's flow channel demonstrates uniformity. However, owing to the interference from the gas phase, the overall pressure of the drainage pump notably decreased when operating under two-phase conditions. Because of the pressure inlet configuration, the inlet static pressure remained constant under varying conditions. In the vicinity of the impeller blades, the rotation of the impeller generated uneven centrifugal forces, leading to an increase in liquid velocity and consequently causing a drop in pressure. As the liquid passed through the impeller blade pressure surface, a local area of high pressure formed near the outer wall. Ultimately, following the guide vane rectification process, the pressure within the outlet flow path of the drainage pump stabilized. In situations where gas was present, the gas-phase interference resulted in the persistence of a localized low-pressure area within the outlet flow path.

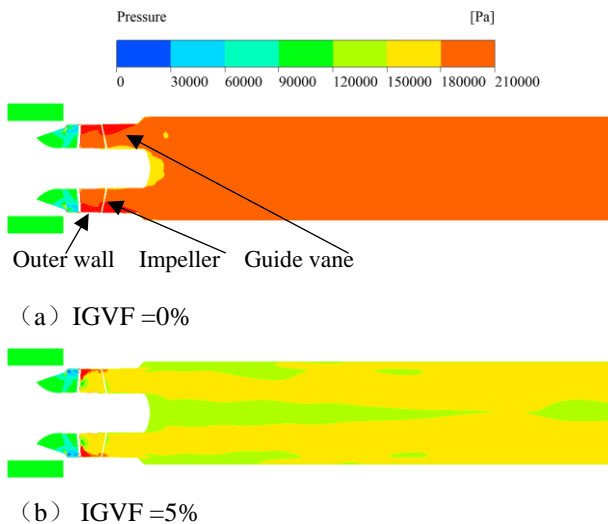


Fig.4 Pressure cloud diagram of middle section

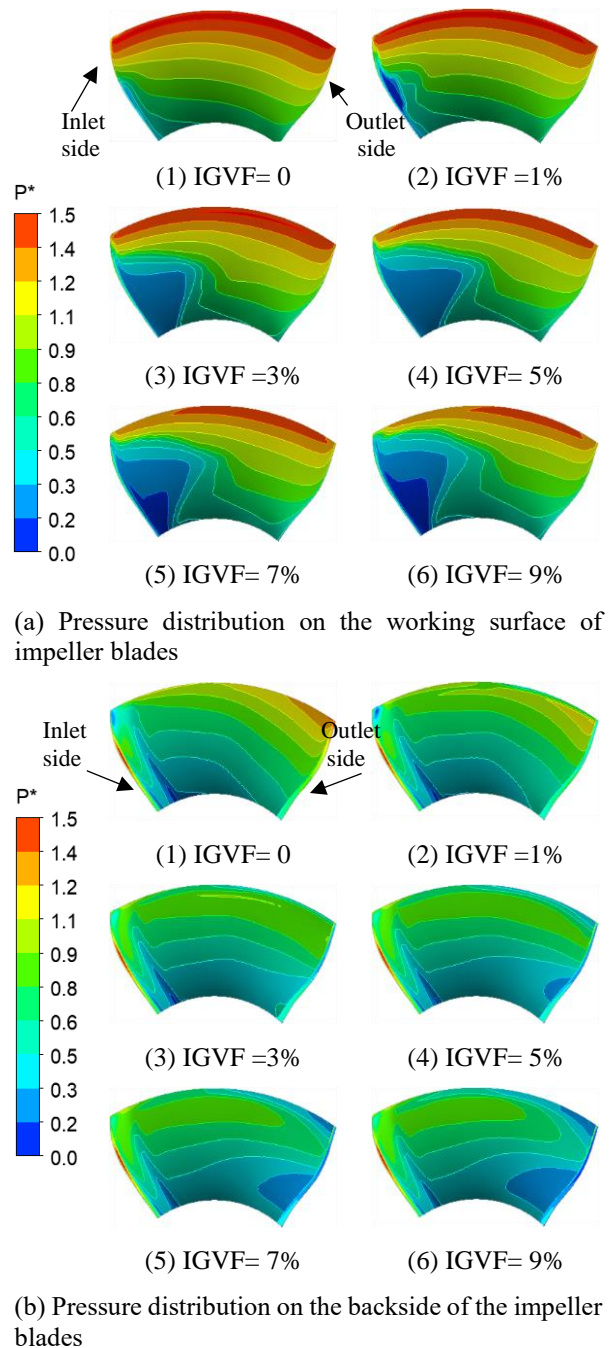


Fig. 5 Impeller blade pressure distribution

Figure 5 presents a comparison of the pressure distribution over the impeller blades under varying gas volume fractions. Since the impeller was responsible for pressurising, it was necessary to determine how the flow of gas and liquid phases influenced the impeller's ability to pressurise. To isolate the effects of fluid density changes on the pressure distribution within the impeller channels, a dimensionless parameter was designated as P^* . $P^* = p / (0.5\rho u_2^2)$, $u_2 = \pi n D_2 / 60$, where, n represents the rotational speed in revolutions per minute (r/min); D_2 is the impeller outlet diameter in meters (m); p denotes total pressure in Pascals (Pa); ρ represents the density in kilograms per cubic meter (kg/m^3); and u_2 signifies the circumferential velocity at the impeller outlet in meters per second (m/s).

Overall, both the similarities and differences in the internal pressure distribution of the drainage pump were noticeable under different conditions. When transporting pure water, the fluid's density and properties remained relatively consistent, leading to a more uniform pressure distribution. However, the presence of gas introduced variations in density and properties, causing fluctuations in the pressure distribution within the pump. As shown in Fig. 5(1), the P^* values on the pressure side increased from the impeller hub towards the impeller's rim, ranging between 0.6 and 1.5. Conversely, the P^* values on the suction side increased from near the impeller hub at the inlet side to near the impeller rim at the outlet side, varying between 0 and 1.4. Under gas content, Figs. 5 (2-6) present the impeller's pressure distribution. As the IGVF (Inlet Gas Volume Fraction) increased, the impeller's pressurization ability weakened, resulting in a reduced area of high-pressure on the blade's pressure side, falling within the range of 1.4-1.5. Additionally, the high-pressure region on the suction side nearly disappears. Figures 5 (a2-a6) illustrate the formation of a low-pressure area on the inlet edge of the pressure side, with P^* values ranging between 0.2-0.3. This area expanded as the IGVF increased and can extend towards the middle of the blade. Notably, at an IGVF of 7%, a small portion of the hub area near the inlet side experienced a P^* value of zero. As shown in Figs. 5 (b2-b6), as the IGVF reached 7%, a small low-pressure region emerged on the suction side near the outlet edge. This occurrence was primarily attributable to the presence of gas bubbles. These bubbles dispersed within the liquid phase, introducing additional flow resistance and significantly disrupting fluid movement. Additionally, the presence of bubbles reduced the average density of the fluid, resulting in relatively lower inertial and frictional forces, thereby diminishing the forces exerted on the blades. Moreover, bubbles had the propensity to adhere to the blades, forming a bubble layer, which also contributed to a decrease in pressure on the impeller blades.

4.2 Streamline Analysis

To observe the flow state of the fluid at different radial heights, the radial coefficient S_p of the blade was defined as the dimensionless distance from the blade hub to the blade rim. $S_p = (r - r_h) / (r_t - r_h)$, where r is the radius, mm; r_t is the rim radius, mm; and r_h is the radius of the hub, mm. The S_p section is shown in Fig. 6.

Figure 7 displays the streamline distribution in cross-sections at different radial heights in different hydraulic components channels. A comparison is provided of the velocity streamlines for pure water and those with varying IGVF values. From Fig. 7(f), an observation can be made that compared to Fig. 7(a), the fluid flow velocity within the pump significantly decreased. At an IGVF of 9%, the fluid velocity within the impeller dropped to the range of 7-14 m/s, while within the guide vane, it decreased to within the range of 0-7 m/s. As the IGVF increased, the similarity of recirculation within the impeller and guide vane decreased, and the vortex structure positions changed. Figure 7 (d) shows that vortices on the suction side of the guide vane reduced near the hub, whereas

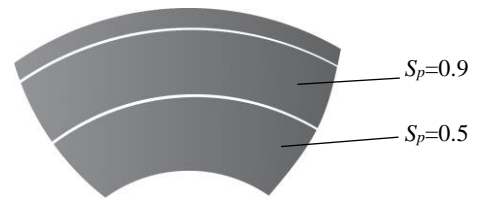


Fig. 6 Section of impeller blade with different radial coefficients S_p

vortices of varying sizes started to emerge on the pressure side. Within the $S_p=0.5$ section, the vortices inside the guide vane underwent continuous deformation, with their scale decreasing as the IGVF increased. The streamline distribution in the guide vane became more regular compared to the condition of those in pure water, as shown in Fig. 7(e). Nevertheless, there was only a slight variation in the streamlines inside the impeller, which was not significant. In contrast to $S_p=0.3$ and $S_p=0.5$, the flow at $S_p=0.9$ section within the guide vane became more stable, with the disappearance of the vortex. Contrastingly, within the impeller, due to the impact of the gap at the rim of the blade, flow separation and a backflow phenomenon occurred near the suction side of the impeller blade. Near the leading edge of the blade, there was a reversal of streamlines, caused by the collision between the main flow and the leakage flow over the blade tip. Overall, as radial coefficients increased, the flow conditions within the impeller deteriorated, while the flow conditions within the guide vane improved, resulting in smaller vortex scales and a more regular overall flow. In the presence of gas, gas content could deteriorate the flow state in the emergency rescue drainage pump, influencing the vortex structure and distribution of positions within the pump to some extent.

4.3 Local Gas Content Distribution

Variations in local gas content directly reflect the distribution of the gas phase within the pump. Figure 8 illustrates the average gas content distribution in various flow components of the drainage pump at different IGVF levels. Overall, the spatial distribution of gas content within the pump exhibited a consistent trend, initially increasing and subsequently decreasing along the direction of flow. The maximum gas content values were attained in close proximity to the impeller and subsequently declined within the guide vane due to the impeller's operational influence. For instance, at an IGVF of 1%, the gas content near the inlet was close to 1%, indicating relatively minimal gas phase accumulation. As the water flowed into the impeller, the gas content increased to approximately 4%, with a noticeable gas phase accumulation phenomenon. Upon entering the guide vane, the average gas content returned to its typical value, slightly higher than that at the inlet. Further, as the IGVF increased, the amplitude of local gas content variations within the flow components became more pronounced. At an IGVF of 9%, the local gas content within the impeller reached as high as 17%, being four times that of the IGVF at 1%. At this point, the local gas content within the guide vane also reached 12%, significantly higher than the gas content at the inlet.

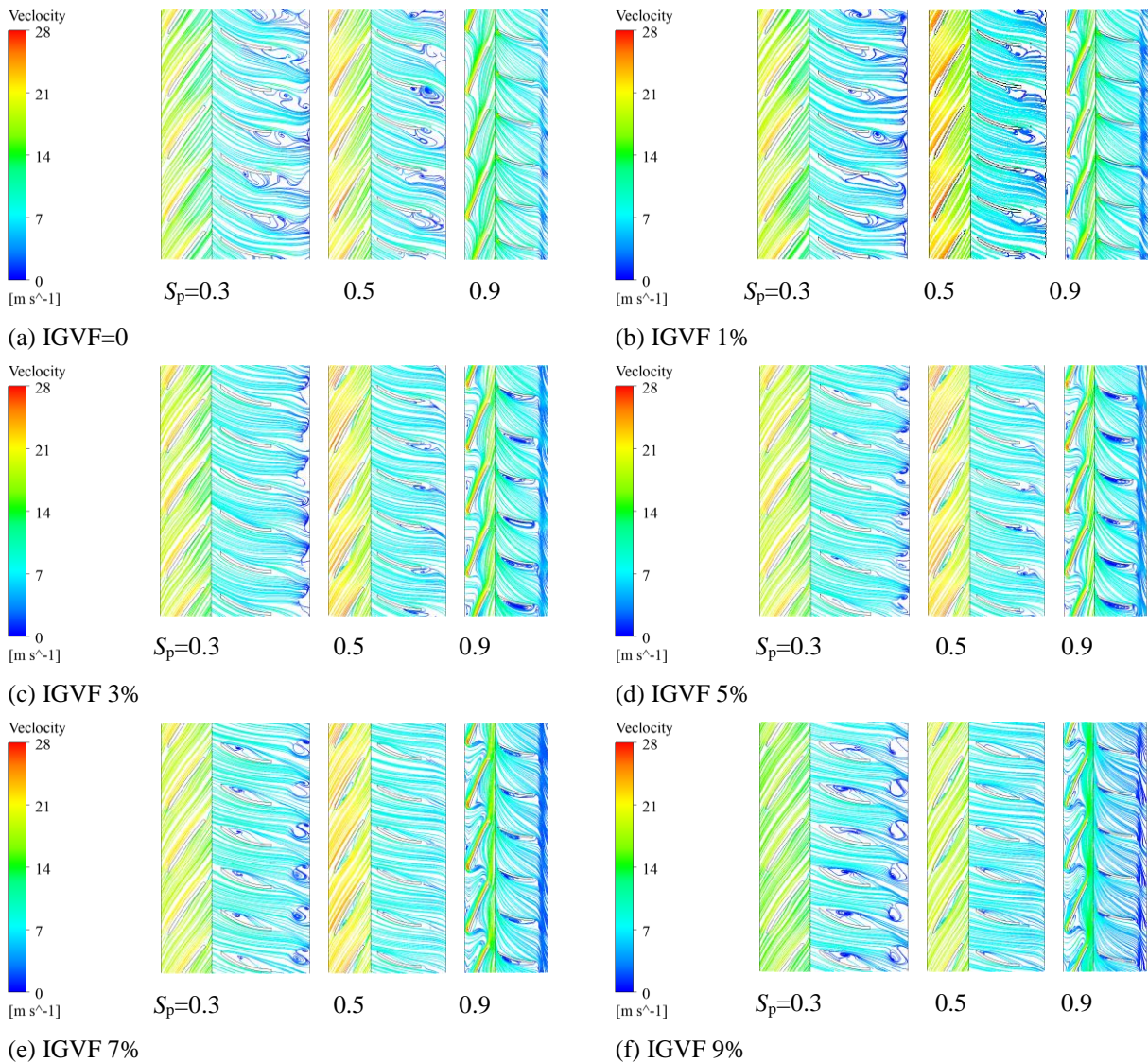


Fig. 7 Liquid streamlines under different IGVFs

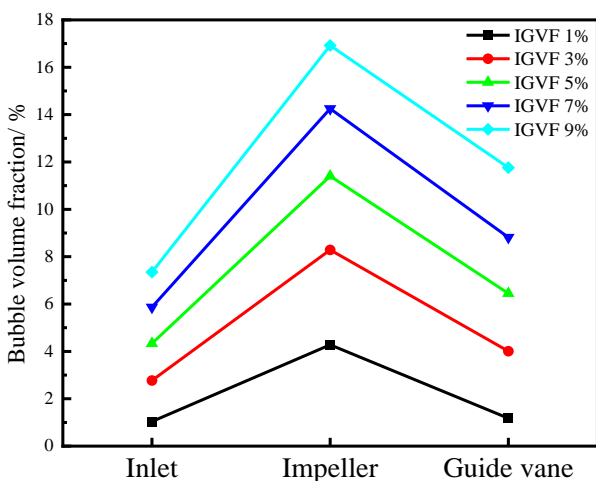
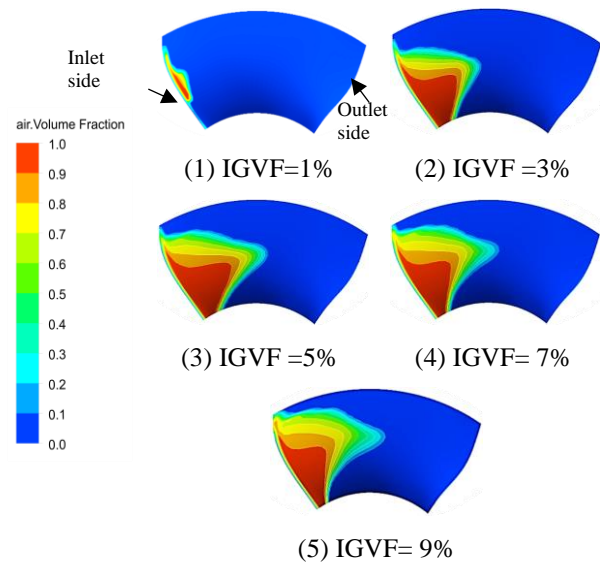


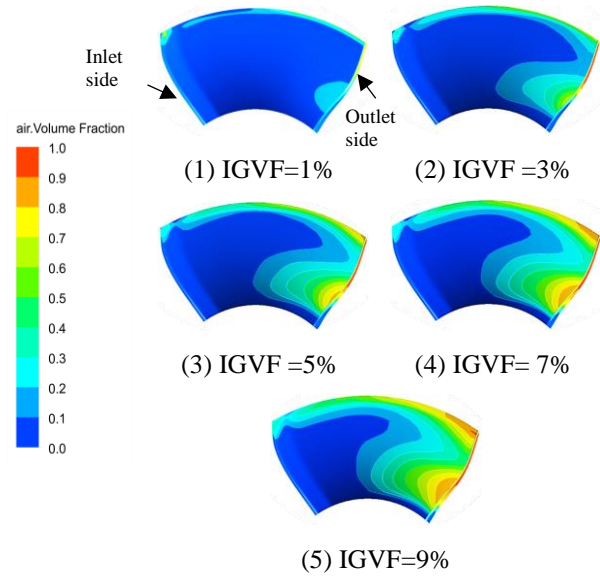
Fig. 8 Average gas content inside the pump

Given that the local gas content within the pump peaked near the impeller, an investigation was undertaken to analyze the distribution of bubbles within the impeller blades. Figure 9 depicts changes in the local gas volume

fraction distribution along the impeller blades as the IGVF increased. As shown in Fig.9 (a), with the IGVF increasing from 1% to 9%, it became evident that gas accumulation occurred prominently at the impeller's pressure side near the inlet edge. Gas volume fractions exceeding 90% could be observed near the inlet edge, and the gas-rich region extended towards the middle and rim of the impeller, forming a gradient distribution. As seen in Figs. 9(a1-a5), when IGVF=1%, bubbles accumulated solely near the inlet edge, while at an IGVF of 9%, bubbles occupied nearly half of the pressure side. As illustrated in Fig. 9(b), the gas phase converged noticeably at the impeller's rim and exit edge on the suction side, and the bubbles extended to the middle section of the impeller as the IGVF increased. As illustrated in Figs. 9(b1-b5), at an IGVF of 1%, the bubbles converged near the rim and exit edge of the impeller on the suction side, albeit with minimal amplitude of convergence, while the gas content remained below 30%. At an IGVF of 9%, the bubbles extended to the impeller's middle section and occupied the entire rim. At the exit edge, the gas content increased significantly, reaching 90%. Overall, Fig. 9 confirms that bubble



(a) gas fraction distribution on impeller pressure side



(b) gas fraction distribution on impeller suction side

Fig. 9 Distribution of gas content on impeller blade

aggregation resulted in steep pressure drops and non-uniform distribution within the impeller, consistent with Fig. 5.

Figure 10 illustrates the gas volume fraction distribution at various annular cross-sections along the impeller. As seen in Figs. 10(a-e), at $S_p=0.3$ and 0.5, fluid experienced gas-liquid separation near the inlet edge of the pressure side of the blades, leading to the accumulation of bubbles towards the middle of the impeller. Once IGVF surpassed 5%, noticeable air pockets formed, with their size increasing with higher IGVF values. At $S_p=0.9$, a significant number of bubbles appeared in the blade passage, with a gas volume fraction exceeding 90%. When IGVF reached 9%, bubbles occupied the whole rim.

4.4 Distribution of Different Bubble Diameter

Figure 11 shows the distribution of AGSF (Air poly. Group i Size Fraction) of gas phase particle groups across various hydraulic components under different IGVF

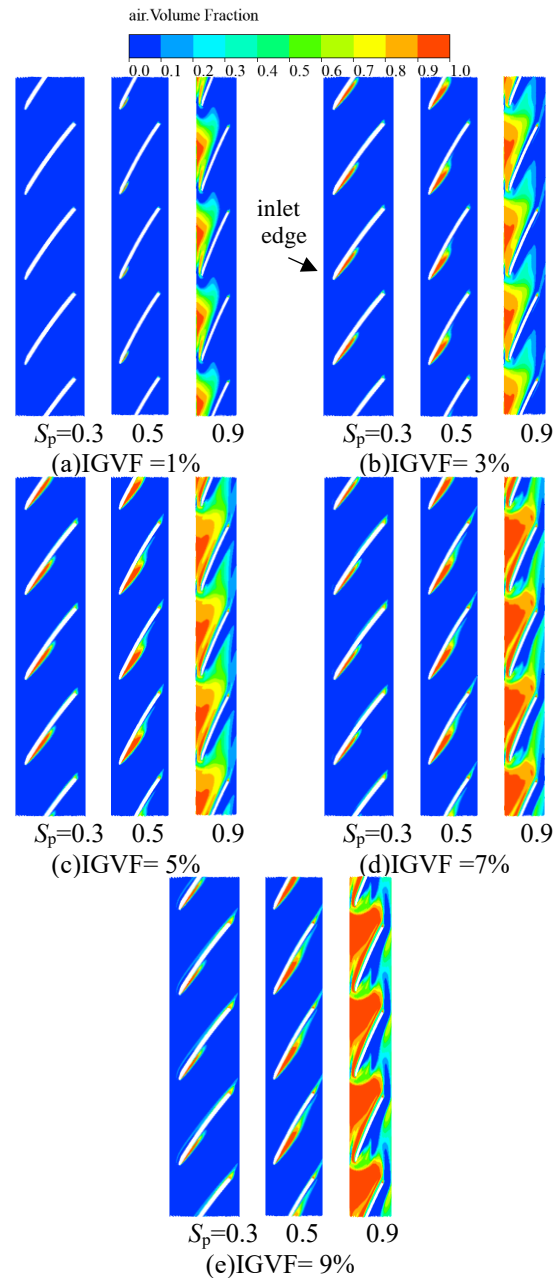
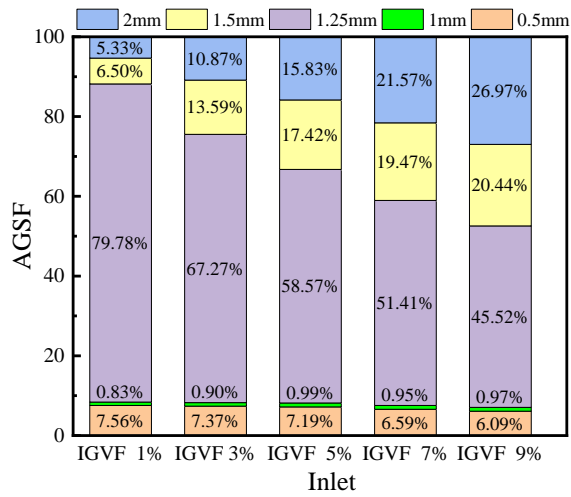
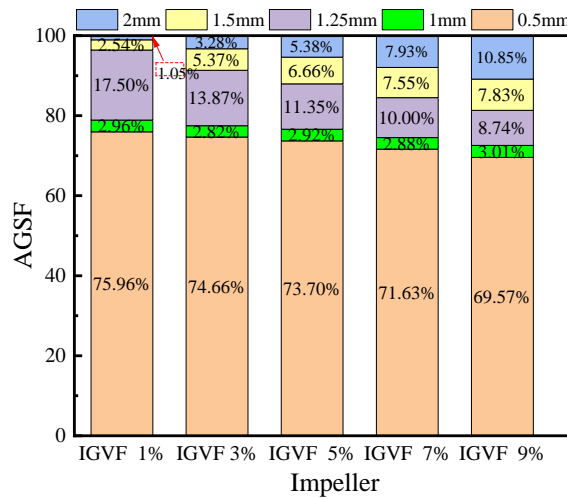


Fig.10 Distribution of gas content at different radial heights

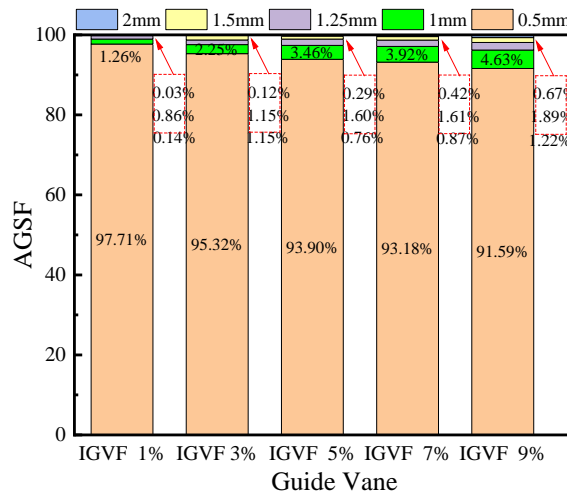
levels. As shown in Fig. 11(a), at the pump inlet, the predominant portion consisted of bubbles with an initial diameter value of 1.25 mm, representing 80% of the total number of bubbles when IGVF=1%. With an increase in IGVF, smaller bubbles tended to coalesce into larger diameter bubbles. Specifically, when IGVF=9%, 1.25 mm bubbles accounted for only 45% of the total, with both 1.5 mm and 2 mm bubbles also comprising 45%. After bubbles entered the impeller, they underwent intense fragmentation due to the impeller's pressurization, fluid shear forces, and the inertia of the bubbles themselves. As shown in Fig. 11(b), within the impeller, 0.5 mm bubbles were predominant, although a notable presence of larger diameter bubbles persists due to the influence of the IGVF. Even at IGVF = 9%, large-size bubbles still accounted for 20% of the total amount of bubbles. Once bubbles entered the guide vane, the fragmentation phenomenon intensified further, with larger-sized bubbles almost entirely breaking



(a) AGSF of Inlet



(b) AGSF of Impeller



(c) AGSF of Guide Vane

Fig. 11 AGSF distribution in hydraulic components

down into 0.5mm bubbles, which accounted for over 90% of the total. Additionally, the overall trend for 1mm diameter bubbles exhibited relatively minor changes. This could be ascribed to their smaller volume and more stable shape, resulting in lower sensitivity to fluid shear forces. As such, the opportunities for rupture and coalescence were comparatively fewer, maintaining a relatively stable overall state. Moreover, when considering a 1.25mm

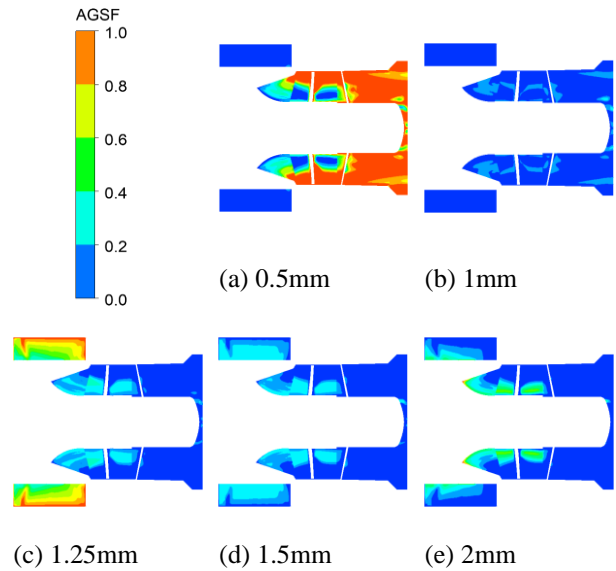


Fig.12 XY=0 cross-section gas-phase particle distribution

initial diameter as the threshold, within the same flow component and under varying IGVF conditions, smaller diameter bubbles exhibited minimal fluctuations, predominantly experiencing fragmentation.

Figure 12 displays the distribution of the gas phase particle group AGSF at the XY=0 section for IGVF=9%. From Fig. 12(c), an observation can be made that as gas entered from the inlet, the flow field experienced lower pressure and relatively lower inter-phase velocities. Consequently, the forces acting on the bubbles were weaker, leading to the tendency for bubble coalescence near the inlet and the formation of larger diameter bubbles. As shown in Fig. 12(a), in proximity to the inlet edge of the impeller, characterized by higher velocity and pressure, bubbles undergo rapid fragmentation, resulting in the formation of smaller diameter bubbles. Figure 12(e) reveals that there were still several bubbles gathering near the hub of the impeller, where the pressure was relatively lower. Large-sized bubbles remained stable. Figure 12(a) also demonstrates that bubbles near the wall of the guide vane primarily existed in smaller diameters. Such findings could be attributed to the higher pressure within the guide vane's internal flow field, resulting in a higher probability of bubble fragmentation.

4.5 Gas Phase Deformation Patterns

The increase in IGVF enhances the clarity of the gas-phase particle diameter distribution graph, providing a more intuitive representation of the gas-phase deformation process. Figure 13 illustrates the average bubble diameter distribution within each hydraulic component of the pump for different IGVF levels. The average bubble diameter is abbreviated as D_{ab} . When IGVF=1%, the D_{ab} decreased from 1.2mm at the inlet to 0.6mm at the impeller, reaching a minimum diameter of 0.5mm at the guide vane. During this phase, the bubbles were exposed to high pressure and the effects of liquid shear, resulting in a crushing speed that exceeded the aggregation speed. Subsequently, after the bubbles entered the outlet pipe, the D_{ab} steeply increased. Due to the rectification effect of the guide vane,

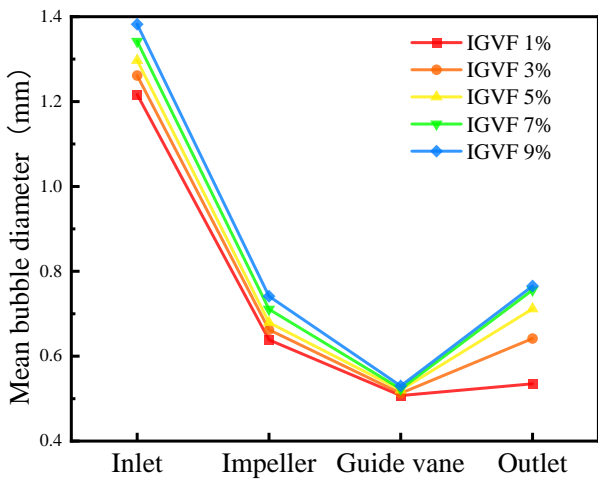


Fig. 13 Mean bubble diameter distribution

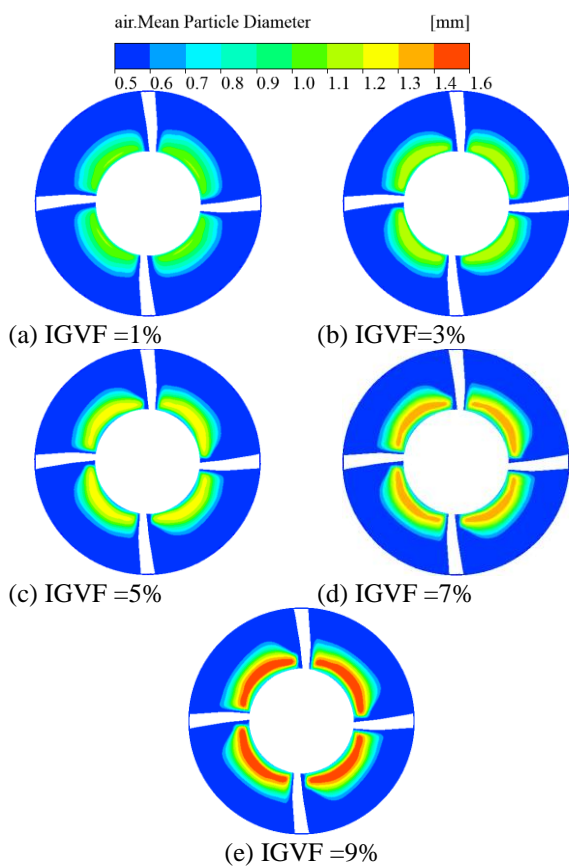
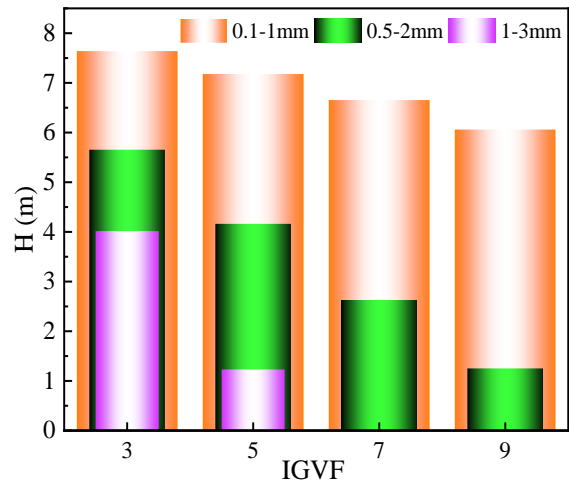


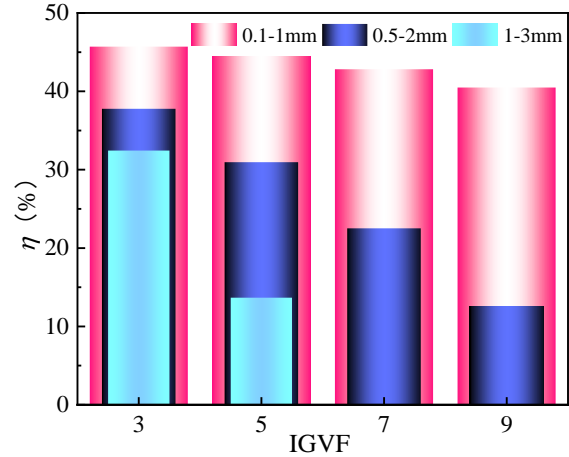
Fig. 14 Bubble diameter distribution in the middle section of the impeller

the liquid flow was smooth, while the bubble aggregation speed was greater than the crushing speed. Further, the mean bubble diameter was influenced by IGVF. When IGVF = 9%, the mean bubble diameters in both the inlet and impeller increased by 0.2 mm compared to when IGVF = 1%. However, within the guide vane, the mean bubble diameter decreased to nearly the same level, with the gas phase being dominated by 0.5 mm bubbles.

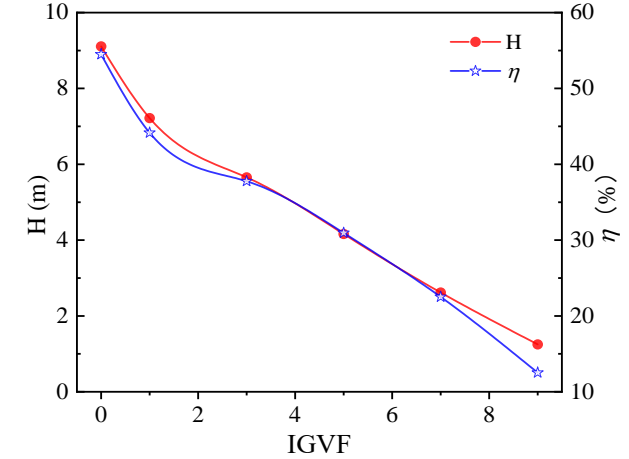
Figure 14 illustrates the variation in the distribution of D_{ab} in the central section of the impeller as IGVF changed. As evidenced, the D_{ab} in the vicinity of the impeller's hub was larger and exhibited a stepwise distribution. Such findings align with the observation made in Fig. 12, which



(a) Variation of head with inlet bubble diameter



(b) Efficiency varies with inlet bubble diameter



(c) When the bubble diameter group 0.5-2mm, head and efficiency with IGVF change curve

Fig. 15 Variation of head and efficiency with IGVF

concluded that larger bubbles tend to accumulate at the impeller's hub due to pressure effects. Specifically, as depicted in Fig. 14(e), as IGVF increased, the D_{ab} within the impeller also increased. When IGVF was set to 9%, the bubble diameter at the hub reached 1.6 mm. This observation is consistent with the conclusion drawn in Fig. 11, indicating that the gas phase's proportion within the pump increased as IGVF increased, with larger-diameter bubbles occupying a greater share.

4.6 Comparison of Hydraulic Performance of Drainage Pumps

The inlet bubble diameter groups of 0.1-1mm, 0.5-2mm, 1-3mm, and the initial bubble diameter of 0.5mm, 1.25mm, and 2mm were selected for three cases to investigate the effect on pump performance. The equations governing the head and efficiency of the drainage pump in the presence of two-phase flow can be expressed as follows:

$$H = \frac{P_{out} - P_{in}}{\rho_{mix} g} \tag{15}$$

$$\eta_t = \frac{9549 * \rho_{mix} g Q H}{T * n} \tag{16}$$

where P_{out} and P_{in} represents the total pressure at the pump outlet and inlet, Pa; ρ_{mix} is the fluid mixture density, kg/m^3 ; T is the torque, $N*m$; and Q is the flow rate, m^3/s .

Figure 15 presents the variations in the head and efficiency of the drainage pump under different IGVF levels and inlet bubble diameter. Figure 15(a) displays the changes in head concerning variations in IGVF and inlet bubble diameter, while Fig. 15(b) presents the efficiency changes under similar conditions. Figure 15(c) focuses on the bubble diameter group ranging from 0.5 to 2mm, showcasing the head and efficiency change curves in response to varying IGVF levels at an inlet diameter of 1.25mm. In general, both the drainage pump head and efficiency exhibited a consistent change trend: as the IGVF and inlet bubble diameter increased, the pump's performance parameters experienced a pronounced reduction. Figures 15(a-b) reveal that when the inlet bubble diameter group fell within the range of 0.1-1mm and the inlet bubble diameter was 0.5mm, the head and efficiency changed slowly as IGVF increased. The pump's performance varied by no more than 15% when compared to conditions at IGVF=3% and IGVF=9%. Under conditions where the inlet bubble diameter group ranged from 1-3mm, specifically with an inlet bubble diameter of 2mm, the head of the pump underwent a significant

reduction of 40%, accompanied by a 10% decrease in efficiency compared to scenarios with a 0.5mm inlet bubble diameter, all observed when the IGVF was set at 3%. Beyond an IGVF of 7%, the head dropped to zero as the bubbles completely obstructed the flow channel, rendering the pump incapable of transferring liquid. Referring to Fig. 15(c), compared to pure water conditions, at IGVF=9%, the pump's head plummeted by 90%, with efficiency declining by nearly 80%, indicating a significant loss in liquid transfer capacity. Conversely, at IGVF levels of 1% and 3%, the changes in head and efficiency occurred more gradually, indicating that the formation of large air pockets obstructing the impeller had not transpired during this interval.

To facilitate a more detailed observation of pressure and D_{ab} fluctuations during the gas-liquid flow within the emergency rescue drainage pump, the following parameter was introduced: H^* , $H^* = (P_i - P_{in}) / (\rho_{mix} g)$. Here, P_i represents the absolute pressure at each axial section (z-x plane) along the emergency rescue and drainage pump's axial direction. Five different conditions, namely IGVF=1%, 3%, 5%, 7%, and 9% were selected. The distribution characteristics of H^* and D_{ab} in the main axis direction are presented in Fig. 16 and Fig. 17, respectively.

Figure 16 illustrates the variation of H^* within the pump along its axial direction for different IGVF levels. As evidenced, there was a negative correlation between the pump's pressure and IGVF. The pressure changes presented similarities and exhibited a hierarchical distribution. Notably, at the junction between the inlet and impeller, the pressure experienced a sharp decline due to static and dynamic interference. For instance, when IGVF was set at 1%, H^* dropped by approximately 2 meters at this location. At the junction of the impeller and guide vane, H^* reached as high as 10 meters when IGVF was set at 1%, and was 6 meters higher than that when IGVF was set at 9%. Finally, following the rectification effect of the guide vane, the pump's pressure steadily decreased, with H^* decreasing by 2 meters for every 2% increase in IGVF.

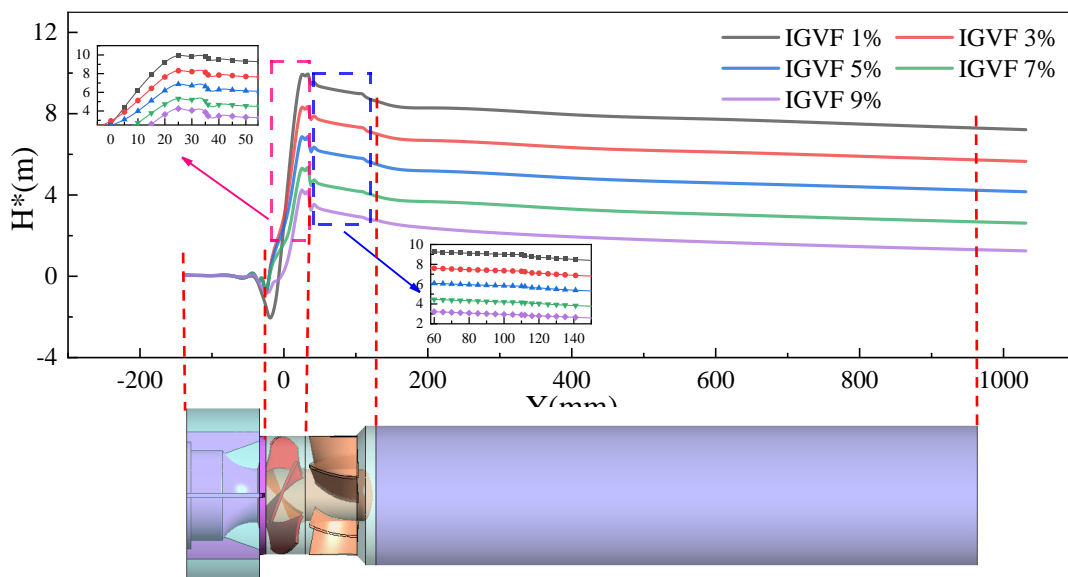


Fig. 16 Variation of H^* in axial direction

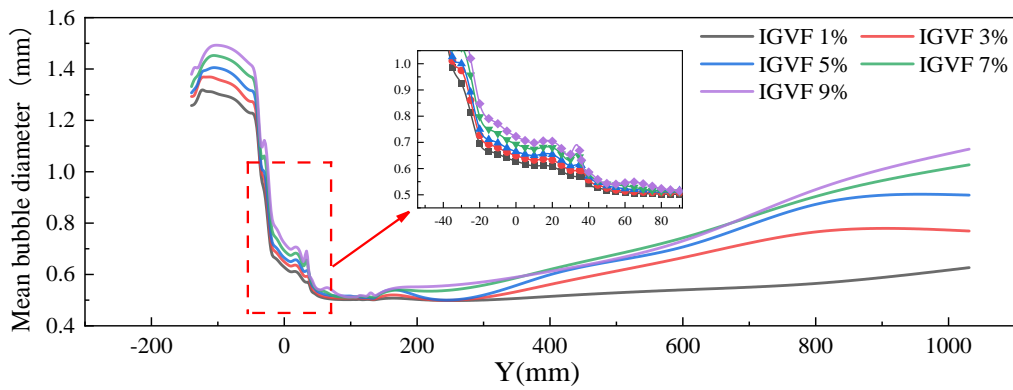


Fig. 17 Variation of mean bubble diameter along the axial direction

Figure 17 illustrates the variation of D_{ab} within the pump along its axial direction for different IGVF levels. There was a positive correlation between the D_{ab} in each region of the pump and the IGVF. Larger bubbles tended to aggregate primarily in the inlet region, where the D_{ab} exceeded the inlet diameter of 1.25mm. Further, the higher the IGVF, the larger the D_{ab} , indicating a tendency towards bubble aggregation. For instance, at IGVF=9%, the D_{ab} was 1.5mm, while at IGVF=1%, the D_{ab} was only 1.3mm. As the bubbles traversed the impeller, the shear effect of the fluid caused a rapid reduction in their average diameter. Large-diameter bubbles underwent fragmentation into smaller ones. As illustrated, the curves exhibited significant overlap near the impeller inlet, indicating a uniform distribution, while demonstrating a cascading pattern within the middle of the impeller. As the flow progressed into the guide vane region, the curves converged almost entirely, suggesting that large-diameter bubbles underwent complete breakdown within the guide vane. Thus, the D_{ab} became concentrated at 0.5mm. In the outlet tube region, there was a tendency for bubbles to accumulate in significant quantities, such as a D_{ab} of 1.1mm observed at IGVF=9%.

4.7 Axial Force Analysis

When the pump impeller rotated at high speed, the primary force sustained by the blades was predominantly axial in nature. In Fig. 18, the axial force on the impeller in one complete rotation cycle was examined at IGVF levels of 3%, 5%, 7%, and 9%, and its variation is presented by using polar coordinates. An observation can be made that over one rotation cycle, the axial force exhibited a periodic distribution characterized by relatively smooth fluctuations. Further, the magnitude of the axial force was directly related to the IGVF level. [Murakami & Minemura \(1974\)](#) highlighted that even a small quantity of bubbles could introduce non-uniformity in flow velocity, prompting deviations in the primary flow direction. This alteration affected the radial velocity of fluid mass points within the impeller, consequently diminishing the magnitude of the radial force. The axial force was greatest and most unstable at IGVF=3%, with fluctuations hovering around 1800N. At IGVF=9%, it fluctuated at 1200N and demonstrated a smoother pattern. This phenomenon can be attributed to the fact that a smaller inlet gas content resulted in relatively more liquid and higher momentum, subjecting the impeller to a larger axial force. Moreover, due to the larger gas-liquid disparity,

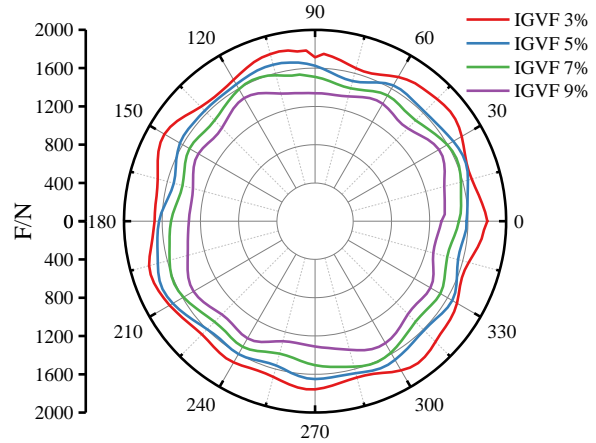


Fig. 18 Axial force polar distribution

bubbles were more prone to rupturing, leading to fluid instability. Further, the axial force under varying gas-liquid conditions displayed multiple sub-peaks and troughs. This suggests that the interaction of gas and high rotational speed may have induced vortex and reflux phenomena inside the impeller, resulting in non-uniform axial forces.

4.8 Ω -Threshold Selection

Typically, the Ω -vortex identification method utilizes a threshold value, commonly falling within the range of 0.50 to 0.65. Vortex structures can be quantitatively characterized by assessing the vortex area, enabling precise tracking of vortex dynamics within the pump across different IGVF levels. For the specific analysis of vortex structures, the condition of IGVF=5% was chosen. Subsequently, the vortex area under different threshold values was compared and a quantitative analysis was conducted to determine the optimal threshold for applying the Ω criterion to the emergency rescue and drainage pump. The change in vortex area with the threshold Ω is depicted in Fig. 19. As evidenced, the vortex area decreased as the threshold Ω increased. $\Omega=0.51$ was chosen as the optimal threshold for the vortex identification method.

4.9 Vortex Identification Analysis Under Different Gas Conditions

To analyze the impact of IGVF on the vortex structure and enhance the differentiation of vortex structures, the Ω

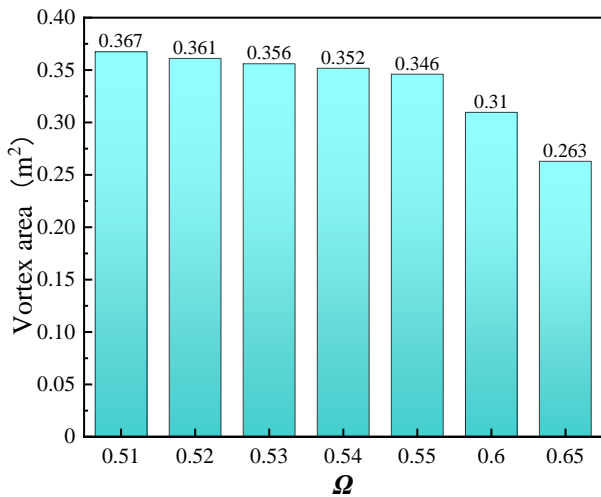


Fig. 19 Variation of vortex area at different thresholds Ω

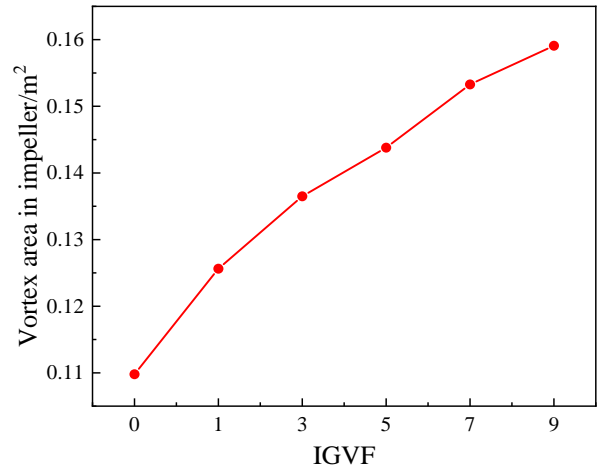


Fig. 21 Vortex area variation within the impeller

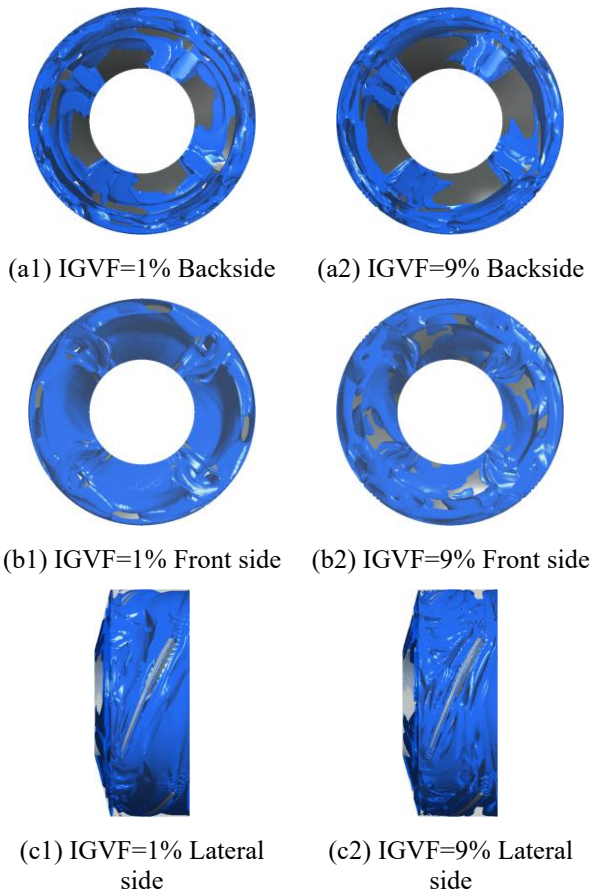


Fig. 20 Vortex structures within the impeller at IGVF=1% and 9%.

method was employed to identify and capture the internal vortex structures of the hydraulic parts at IGVF=1% and 9%. For the remaining IGVF conditions, the vortex structures were represented by vortex areas.

Figure 20 presents the vortex structure identification within the axial impeller. Under different IGVF levels, there were both similarities and differences in the

localized vortex patterns. These vortex structures predominantly consisted of inlet recirculation vortices, blade surface separation vortices, and gap leakage vortices. In comparison to Fig. 20(a) at IGVF=1%, Fig. 20(b) at IGVF=9% displays a significantly larger area on both the pressure and suction sides of the impeller that lacks vortex coverage. This observation aligns with the bubble accumulation regions investigated earlier, indicating that a considerable number of bubbles adhered to the blade surface. Additionally, Fig. 20(c) reveals that at IGVF=9%, there was a significant increase in vortices at the blade exit, with vortices occupying the entire gap near the rim. Further, the vortex structure became more intricate.

Figure 21 illustrates the variation in vortex area within the impeller at different IGVF levels. An observation can be made that as IGVF increased, the vortex area within the impeller also increased. At IGVF=9%, the vortex area increased by 0.05m² compared to IGVF=0%. Further, the initial introduction of gas phase had a more pronounced impact on the vortex patterns within the impeller compared to increasing gas content. The curve from 0% to 1% IGVF exhibited a steeper slope.

Figure 22 presents the vortex structure identification within the guide vane. The vortices within the guide vane were primarily composed of inlet separation vortices, passage vortices, and outlet recirculation vortices. As depicted in Fig. 22(a), the vortices primarily concentrated on the blade surfaces and within the channels. In Fig. 22(b), compared to IGVF=1%, under IGVF=9%, an expanding vortex structure became evident. Further, the coherent vortex structure observed at IGVF=1% was disrupted by the presence of bubbles, breaking into irregularly distributed smaller segments. Close to the exit of the guide vanes, vortex patterns exhibited a degree of regularity owing to the constraints imposed by the hub shape, leading to circumferential motion around the guide vane. Figure 22(c) illustrates that increasing IGVF significantly impacted the vortices within the guide vane channels. Under IGVF=9%, vortices occupied almost the entire circumferential portion of the guide vane channels.

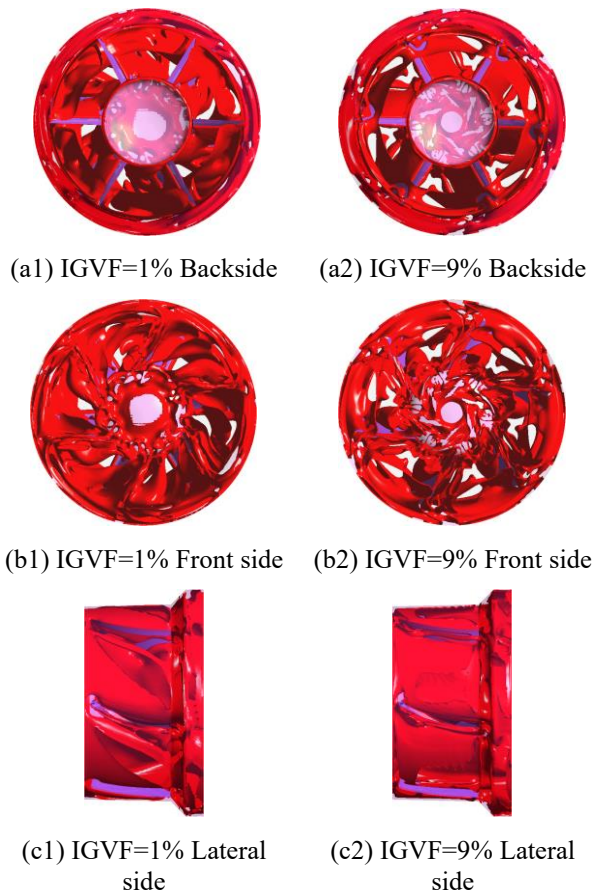


Fig. 22 Vortex structures within the guide vane under IGVF=1% and 9%

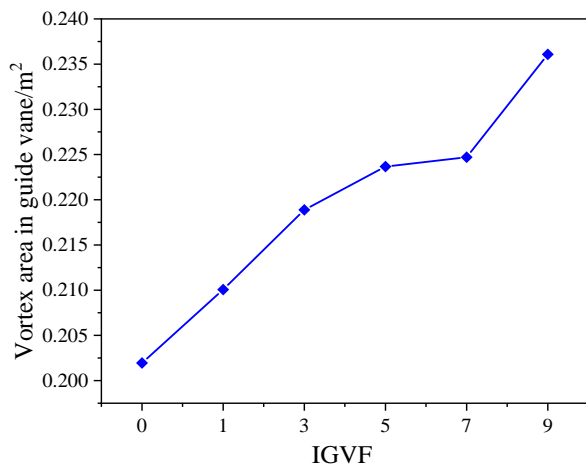


Fig. 23 Vortex area variation within the guide vane

Figure 23 illustrates the variation in vortex area within the guide vane at different IGVF levels. The trend in changes of vortex area mirrors what was observed within the impeller, showing a notable surge in vortex area between IGVF=7% and IGVF=9%, where the area escalated from 0.225 m² to 0.357 m². Generally, as the IGVF increased, the vortex area within the drainage pump also increased.

5. CONCLUSIONS

Numerical simulations of multiphase flow within the emergency rescue drainage pump were conducted based on the MUSIG model. The research findings can be summarized as follows:

(1) The performance of the drainage pump progressively deteriorated as IGVF increased. The disruption of liquid-phase streamlined and the intensity of backflow exacerbated, resulting in a notable gas accumulation phenomenon. This occurrence was particularly prominent near the impeller's inlet on the pressure side and near the rim on the suction side. Moreover, when the IGVF reached 7%, gas pockets formed within the flow channel.

(2) Within the annular inlet, bubbles remained relatively stable and tended to aggregate. Following passage through the impeller, bubbles undergo significant fragmentation, breaking down into the smallest possible diameter. This process led to a high concentration of small bubbles near the impeller's rim. As the bubbles traversed the guide vane, further fragmentation occurred, with small bubbles predominantly adhering to the surfaces of the guide vane blades. Ultimately, within the outlet pipe, these bubbles coalesced into larger diameters. Under equivalent IGVF conditions, the larger the initial diameter of bubbles, the more detrimental the pump performance.

(3) In terms of gas content, the vortex structures within the impeller and guide vane were predominantly characterized by blade separation vortices and inter-blade leakage vortices. Vortices within the impeller concentrated near the blade exit and the rim, while those within the guide vane were mainly composed of blade vortex. As IGVF increased, the vortex area continuously expanded, resulting in more intricate vortex structures. The vortices within the guide vane became fragmented into multiple smaller segments. Further, gas phase accumulation significantly influenced backflow, vortex instability, and other unstable flow phenomena.

ACKNOWLEDGEMENTS

This work was supported by National Key Research and Development Program (Grant No. 2020YFC1512405) and Jiangsu Provincial Key Research and Development Program (Grant No.BE2020330).

CONFLICT OF INTEREST

The authors have no competing interests or conflicts to disclose.

AUTHORS CONTRIBUTION

Cao Weidong and **Yang Xinyu**: Conceptualization; methodology; formal analysis; writing – original draft; **Wang He** and **Leng Xinyi**: writing–review & editing. All authors have read and agreed to the published version of the manuscript.

REFERENCES

- Chen, Y., Patil, A., Chen, Y., Bai, C., Wang, Y., & Morrison, G. (2019). Numerical study on the first stage head degradation in an electrical submersible pump with population balance model. *Journal of Energy Resources Technology*, 141(2), 022003. <https://doi.org/10.1115/1.4041408>
- Chong, M. S., Perry, A. E., & Cantwell, B. J. (1990). A general classification of three-dimensional flow fields. *Physics of Fluids A: Fluid Dynamics*, 2(5), 765-777. <https://doi.org/10.1063/1.857730>
- Kim, J. H., Lee, H. C., Kim, J. H., Choi, Y. S., Yoon, J. Y., Yoo, I. S., & Choi, W. C. (2015). Improvement of hydrodynamic performance of a multiphase pump using design of experiment techniques. *Journal of Fluids Engineering*, 137(8), 081301. <https://doi.org/10.1115/1.4029890>
- Levy, Y., Degani, D., & Seginer, A. (1990). Graphical visualization of vortical flows by means of helicity. *AIAA Journal*, 28(8), 1347-1352. <https://doi.org/10.2514/3.25224>
- Li, Z., Wang, D., Li, D., & Li, Q. (2023). Energy loss characteristics of pump turbine runner based on entropy generation and vorticity. *Journal of Drainage and Irrigation Machinery Engineering*, 41(6), 541-548. <https://doi.org/10.3969/j.issn.1674-8530.21.0304>
- Liu, C., Wang, Y., Yang, Y., & Duan, Z. (2016). New omega vortex identification method. *Science China Physics, Mechanics & Astronomy*, 59, 1-9. <https://doi.org/10.1007/s11433-016-0022-6>
- Liu, M., Tan, L., & Cao, S. (2022). Theoretical prediction model of gas-phase diameter in multiphase pump based on Weber number. *Journal of Drainage and Irrigation Machinery Engineering*, 40(08), 793-799. <https://doi.org/10.3969/j.issn.1674-8530.21.0370>
- Lo, S. (1996). Application of the MUSIG model to bubbly flows. *AEAT-1096, AEA Technology*, 230(8216), 826.
- Luo, H., & Svendsen, H. F. (1996). Theoretical model for drop and bubble breakup in turbulent dispersions. *AIChE Journal*, 42(5), 1225-1233. <https://doi.org/10.1002/aic.690420505>
- Murakami, M., & Minemura, K. (1974). Effects of entrained air on the performance of centrifugal pumps: 2nd report, effects of number of blades. *Bulletin of JSME*, 17(112), 1286-1295. <https://doi.org/10.1299/jsme1958.17.1286>
- Pineda, H., Biazussi, J., López, F., Oliveira, B., Carvalho, R. D., Bannwart, A. C., & Ratkovich, N. (2016). Phase distribution analysis in an Electrical Submersible Pump (ESP) inlet handling water-air two-phase flow using Computational Fluid Dynamics (CFD). *Journal of Petroleum Science and Engineering*, 139, 49-61. <https://doi.org/10.1016/j.petrol.2015.12.013>
- Prince, M. J., & Blanch, H. W. (1990). Bubble coalescence and break-up in air-sparged bubble columns. *AIChE Journal*, 36(10), 1485-1499. <https://doi.org/10.1002/aic.690361004>
- Wang, L., Lu, J., Liao, W., Zhao, Y., & Wang, W. (2019). Numerical simulation of the tip leakage vortex characteristics in a semi-open centrifugal pump. *Applied Sciences*, 9(23), 5244. <https://doi.org/10.3390/app9235244>
- Wu, Y. L., Gao, S., & Ge, L. (1998, October). *Three-dimension calculation of oil-bubble flows through a centrifugal Pump impeller*. Proceedings of the Third Internal Conference on Pump and Fan, Beijing, China.
- Xu, Z., Li, Z., Wang, W., W, Q., & Xu, Y. (2023). Influence of air void fraction on pressure fluctuation of centrifugal aviation fuel pump blade. *Journal of Drainage and Irrigation Machinery Engineering*, 41(03), 239-246. <https://doi.org/10.3969/j.issn.1674-8530.21.0256>
- Yan, S., Sun, S., Luo, X., Chen, S., Li, C., & Feng, J. (2020). Numerical investigation on bubble distribution of a multistage centrifugal pump based on a population balance model. *Energies*, 13(4), 908. <https://doi.org/10.3390/en13040908>
- Zhang, F., Zhu, L., Chen, K., Yan, W., Appiah, D., & Hu, B. (2020a). Numerical simulation of gas-liquid two-phase flow characteristics of centrifugal pump based on the CFD-PBM. *Mathematics*, 8(5), 769. <https://doi.org/10.3390/math8050769>
- Zhang, F., Appiah, D., Chen, K., Yuan, S., Adu-Poku, K. A., & Wang, Y. (2020b). Dynamic characterization of vortex structures and their evolution mechanisms in a side channel pump. *Journal of Fluids Engineering*, 142(11), 111502. <https://doi.org/10.1115/1.4047808>
- Zhou, J., Adrian, R. J., Balachandar, S., & Kendall, T. (1999). Mechanisms for generating coherent packets of hairpin vortices in channel flow. *Journal of Fluid Mechanics*, 387, 353-396. <https://doi.org/10.1017/S002211209900467X>